IEEE Access
Multidisciplinary | Rapid Review | Open Access Journal

Received 8 September 2023, accepted 17 September 2023, date of publication 25 September 2023,
date of current version 9 October 2023.

Digital Object Identifier 10.1109/ACCESS.2023.3319047

RESEARCH ARTICLE

Design and Analysis of Novel Modular Stator Axial-Flux Permanent Magnet Vernier Machine With Improved Power Factor

GONGDE YANG[1,2], JIE LI[1,2], AND MINGYAO LIN[3], (Member, IEEE)
[1]School of Electrical Engineering and Automation, Fuzhou University, Fuzhou 350108, China
[2]Fujian Key Laboratory of New Energy Generation and Power Conversion, Fuzhou University, Fuzhou 350108, China
[3]School of Electrical Engineering, Southeast University, Nanjing 210000, China

Corresponding author: Gongde Yang (gdyang@fzu.edu.cn)

This work was supported in part by the National Natural Science Foundation of China under Project 52107039, and in part by the Natural Science Foundation of Fujian Province under Project 2021J05133.

ABSTRACT Permanent magnet Vernier machines (PMVMs) have drawn increasing attention in recent years due to the advantage of high torque density. However, the inherent low power factor issue of PMVMs remains a key challenge. In this paper, a novel axial-flux permanent magnet vernier machine (AFPMVM) with modular stator is proposed. Benefiting from the unique separation slot structure, the proposed machine can obtain not only the improved power factor but also the higher electromagnetic torque, and this is explained theoretically by air-gap field modulation theory. A magnetomotive force (MMF)-permeance model is established to predict the air-gap field harmonics modulated by the stator slots. Moreover, by quantifying the contribution of air-gap field harmonics to the torque generation, the working and non-working harmonic components of the air-gap field in the proposed machine can be determined. Meanwhile, the relationship between electromagnetic torque and power factor of the proposed AFPMVM is revealed from the perspective of the air-gap field harmonics. Then, the power factor of the proposed machine is significantly improved due to the lower non-working harmonic contents of armature reaction field. The analysis results show that the proposed AFPMVM can achieve 4.1% higher electromagnetic torque and 6.9% higher power factor than the existing AFPMVM. Finally, the influences of some key design parameters on electromagnetic torque and power factor of the proposed AFPMVM are analyzed and verified by finite element analysis.

INDEX TERMS Axial flux, electromagnetic torque, field modulation, permanent magnet (PM) vernier machine, power factor.

I. INTRODUCTION

Due to the inherent merit of high torque density and simple mechanical structure, permanent magnet (PM) vernier machines (PMVMs) have received increasing attention and have become promising candidate for direct-drive applications such as ship propulsion, wind power generation, and electric vehicle, etc. [1], [2], [3], [4]. Significant works on the magnetic gearing effect of the PMVM have been presented in [5], [6], [7], and [8], which reveal that the PMVM exhibits higher output torque than that of the regular PM synchronous machine (PMSM) with the modulation effect of stator teeth. Besides, many novel PMVM topologies have been proposed to further improve output torque, such as consequent pole rotor PMVM [9], double-rotor PMVM [10], double-excitation PMVM [11], and split-tooth PMVM [12], etc.

In order to select proper slot/pole combination to acquire relatively high torque density, the influence of different slot/pole combinations on the electromagnetic performance of PMVMs is evaluated in [13], which reveals that the PMVMs with high pole ratio (pole-pair number ratio of PM rotor to armature winding) have the merit of high torque density. However, PMVMs with high pole ratio generally

The associate editor coordinating the review of this manuscript and approving it for publication was Feifei Bu.

suffer from relatively low power factor, resulting in increased requirement of inverter capacity and higher cost [14], [15], [16]. This is mainly because the leakage flux and armature reaction reactance of PMVMs will increase with the increase of pole-pair number (PPN) of PMs [17]. Recently, numerous research works have been conducted to improve the power factor by increasing PM flux linkage [18], [19]. In [20], the spoke-type PMVM is investigated to enhance the PM flux linkage and power factor with the aid of the flux focusing effect, while the torque density is weakened by the unique flux barrier. To overcome the flux barrier issue and further improve the power factor, a double-stator spoke-type PMVM is proposed, which provides a flux bridge between two stators to improve the flux path and PM flux density. As a result, the power factor and torque density are both improved [21]. However, this machine with two-layer air-gaps suffers from issues of mechanical complexity and reliability. Besides, due to the limitations caused by the property of PM material, it is actually far from to improve the power factor of the PMVM only by increasing PM flux linkage. Thus, the way to reduce armature reaction flux linkage has been identified as alternative method. In [22], a PMVM with modular stator and yokeless rotor is proposed to improve power factor by weakening the armature reaction flux linkage. A PMVM with coil pitch of two slot pitches is presented in [23]. The power factor of the PMVM can be improved to a certain extent, whereas its torque density is uncompetitive. It means that the armature reaction field is closely related to the torque density and power factor.

Generally, integral slot distributed windings (ISDWs) featured by longer end-winding are mostly adopted in PMVMs, which may significantly increase the machine volume and offset the advantage in torque density. To shorten end-winding length and reduce copper usage, the PMVMs with fractional slot concentrated windings (FSCWs) have been investigated in [24], [25], [26], and [27]. It should be noted that the FSCW structure typically generates abundant armature reaction magnetomotive force (MMF) harmonics. Based on the air-gap field modulation theory, the effective armature reaction field harmonics play a crucial role in the research of the PMSM torque generation mechanism [28], [29], [30]. Meanwhile, there is a conflicting relationship between electromagnetic torque and power factor of PMVMs. Therefore, analyzing the relationship between torque density and power factor from the perspective of the armature reaction field harmonics is of great significance for PMVMs to improve power factor and maintain high torque density.

In this paper, a novel axial-flux PMVM (AFPMVM) with separation slots in the stator is proposed. The relationship between electromagnetic torque and power factor of the proposed AFPMVM is revealed from the perspective of air-gap field harmonics. The separation slots of the proposed AFPMVM can not only work as magnetic barriers to separate magnetic circuits, but also provide non-uniform distributed field modulation poles (FMPs) to generate additional permeance harmonics. Thus, the armature reaction MMF can be modulated to produce a higher proportion of the armature reaction field working harmonic. With the help of the stator separation slot structure, the proposed AFPMVM can obtain improved power factor and higher torque density.

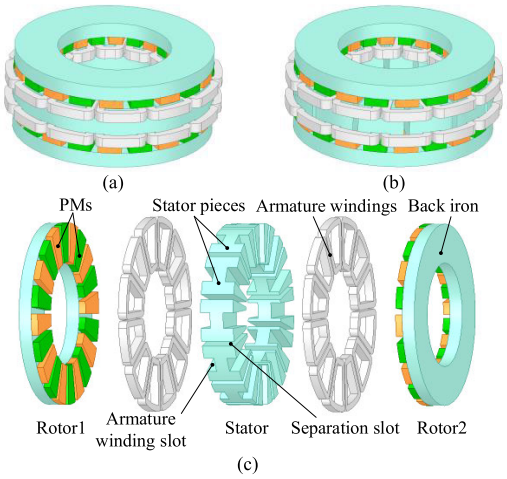

FIGURE 1. Configurations of machines. (a) Existing AFPMVM. (b) Proposed AFPMVM. (c) Exploded view of the proposed AFPMVM.

The rest of this paper is organized as follows: the topology of the proposed AFPMVM will be introduced in Section II. In Section III, an MMF-permeance model will be established to predict the air-gap field harmonics accounting for air-gap field modulation effect. In Section IV, in order to investigate the relationship between the electromagnetic torque and power factor of the proposed AFPMVM, the working and non-working harmonic components of the air-gap field will be further determined. Furthermore, the influences of key design parameters on the output torque and power factor of the proposed AFPMVM will be investigated in Section V. Finally, some conclusions will be drawn in Section VI.

II. MACHINE TOPOLOGIES

The configuration of the existing AFPMVM is shown in Fig. 1(a), which has dual identical surface-mounted PM rotors and one armature stator sandwiched in between [31]. The axially magnetized PMs on the two back irons are circumferential symmetric and have opposite polarity. The armature winding adopts double-layer FSCWs for reducing end-winding length. Fig. 1(b) and (c) present the configuration of the proposed AFPMVM. It can be seen that the difference between these machines lies in the structure of the stator core. For the proposed AFPMVM, the FSCWs are embedded into the slots of adjacent H-type modular stator pieces. Meanwhile, the non-uniform distribution of FMPs caused by the separation slot structure in the proposed machine is beneficial for improving the air-gap field modulation effect.

Fig. 2 shows the parametric model of the proposed AFPMVM. To reduce the manufacture difficulty, the parallel armature winding slot and parallel separation slot stator is applied to the proposed AFPMVM as shown in Fig. 2(b). However, due to the parallel stator slot structure, the ratio of

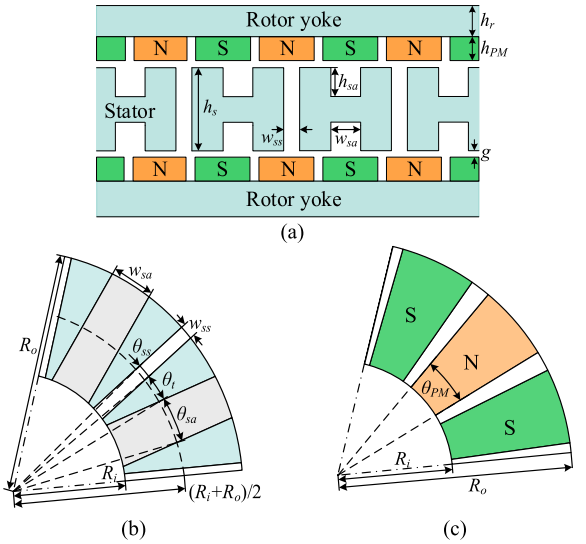

FIGURE 2. Parametric model of the proposed AFPMVM. (a) Cross-sectional view. (b) Top view of the stator. (c) Top view of the rotor.

TABLE 1. Main parameters of existing machine and proposed machine.

Item and symbol	Existing AFPMVM	Proposed AFPMVM
Armature winding slot number, N_a	12	12
PM rotor pole-pair, P_r	10	10
Separation slot number, N_s	12	12
Stator outer radius, R_o (mm)	52.5	52.5
Stator inner radius, R_i (mm)	30	30
Stator axial length, h_s (mm)	20	20
Back iron thickness, h_r (mm)	7.5	7.5
PM pole-arc coefficient, θ_{PM}	0.759	0.759
PM thickness, h_{PM} (mm)	4	4
PM material	NdFeB	NdFeB
Armature winding slot width, w_{sa} (mm)	10.4	10.4
Armature winding slot depth, h_{sa} (mm)	6	6
Separation slot width, w_{ss} (mm)	/	3
Rated current, I_a (A)	5	5
Number of turns per phase	80	80
Air-gap length, g (mm)	0.25	0.25

armature winding slot width w_{sa} and separation slot width w_{ss} to slot pitch of the proposed machine decrease with the decrease of air-gap radius. Hence, it is necessary to introduce the coefficients θ_{ss}, θ_t, and θ_{sa} at the average radius of the air-gap to investigate the air-gap field modulation effect of the proposed machine, in which θ_{ss}, θ_t, and θ_{sa} represent the separation slot arc, stator tooth arc and armature winding slot arc, respectively. The main design parameters are tabulated in Table 1.

It should be noted that the separation slot structure only causes non-uniform distribution of FMPs and does not change the PPN of FMPs. In other words, the effective harmonic order of the armature reaction field of the proposed AFPMVM is the same as that of the existing AFPMVM. Thus, the proposed AFPMVM with separation slot shares the same operation principle of the air-gap field modulation as that of the existing AFPMVM and the relationships of armature winding slot number N_a, armature winding pole-pair P_a, and

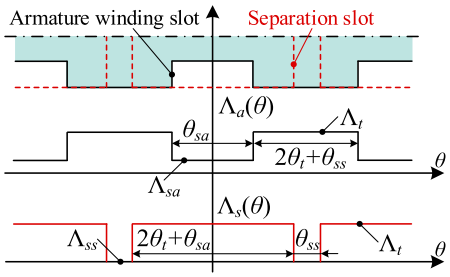

FIGURE 3. The simplified linearized air-gap permeance model of the proposed AFPMVM.

PM rotor pole-pair P_r can be expressed as

$$P_a = N_a - P_r \tag{1}$$

III. AIR-GAP FIELD MODULATION PRINCIPLE

In this section, the harmonic generation and variation mechanisms in the air-gap field of the proposed AFPMVM are revealed by the air-gap field modulation theory, which lays the foundation for studying the relationship between the air-gap field harmonics and electromagnetic performances. In order to obtain a simplified analytical model for air-gap flux density, some assumptions are made as follows.

1) The permeances of the H-type modular stator pieces and rotor back irons are considered infinite, so as to the saturation effect of the iron core can be ignored.
2) The relative permeability of PMs is the same as that of vacuum.
3) The leakage flux is ignored for simplicity.

A. AIR-GAP PERMEANCE MODULATION FUNCTION

Different from the existing AFPMVM with uniform distributed armature winding slot, in the proposed AFPMVM, not only do the armature winding slots serve as FMPs to generate air-gap permeance harmonics, but the separation slots also work as FMPs to further adjust the distribution of air-gap permeance harmonics. Based on the air-gap field modulation theory, the air-gap permeance modulation behavior of the proposed AFPMVM can be divided into two parts, namely, armature winding slot modulation function $\Lambda_a(\theta)$ and separation slot modulation function $\Lambda_s(\theta)$. Therefore, the simplified linear air-gap permeance model of the proposed machine can be obtained by establishing a coordinate system with the center of the armature winding slot as the origin, as shown in Fig. 3.

According to the armature winding slot permeance model shown in Fig. 3, the armature winding slot modulation function can be deduced by

$$\Lambda_a(\theta) = \Lambda_{a0} + \sum_{v=1,2,3\ldots}^{\infty} \Lambda_{av} \cos(vN_a\theta) \tag{2}$$

where θ is the air-gap circumferential position, Λ_{a0} and Λ_{av} are the dc component and amplitude of the vth harmonic of armature winding slot permeance, respectively. Λ_{a0} and Λ_{av}

can be expressed as

$$\Lambda_{a0} = \frac{N_a \left[\Lambda_{sa}\theta_{sa} + \Lambda_t \left(2\theta_t + \theta_{ss}\right)\right]}{2\pi} \tag{3}$$

$$\Lambda_{av} = \frac{2\left(\Lambda_{sa} - \Lambda_t\right)}{v\pi} \sin\left(\frac{vN_a\theta_{sa}}{2}\right) \tag{4}$$

where Λ_{sa} and Λ_t are the amplitudes of air-gap permeance at the circumferential position of the armature winding slot and stator tooth, respectively. It should be noted that the armature winding slot modulation function can be regarded as the same as the air-gap permeance modulation function of the existing AFPMVM. By using a stator without armature winding slots, the separation slot modulation function can be obtained and expressed as

$$\Lambda_s\left(\theta\right) = \Lambda_{s0} + \sum_{v=1,2,3\ldots}^{\infty} \Lambda_{sv} \cos\left[vN_s\left(\theta + \frac{\pi}{N_a}\right)\right] \tag{5}$$

where N_s is the number of the separation slot, Λ_{s0} and Λ_{sv} are the dc component and amplitude of the v^{th} harmonic of separation slot permeance, respectively. These coefficients can be determined by

$$\Lambda_{s0} = \frac{N_s \left[\Lambda_{ss}\theta_{ss} + \Lambda_t \left(2\theta_t + \theta_{sa}\right)\right]}{2\pi} \tag{6}$$

$$\Lambda_{sv} = \frac{2\left(\Lambda_t - \Lambda_{ss}\right)}{v\pi} \sin\left[vN_s\left(\frac{2\theta_t + \theta_{sa}}{2}\right)\right] \tag{7}$$

where Λ_{ss} is the amplitude of air-gap permeance at the circumferential position of the separation slot.

The air-gap permeance modulation function of the proposed AFPMVM can be derived by the product of the modulation functions of the armature winding slot and separation slot. Nevertheless, since $\Lambda_a(\theta)$and $\Lambda_s(\theta)$ are even functions with the half period phase difference and same period, the air-gap permeance modulation function can be expressed as

$$\Lambda\left(\theta\right) = \Lambda_0 + \sum_{v=1,2,3\ldots}^{\infty} \Lambda_v \cos\left(vN_a\theta\right) \tag{8}$$

where Λ_0 and Λ_v are the dc component and amplitude of the v^{th} harmonic of air-gap permeance modulation function, respectively.

Fig. 4 shows the air-gap permeance harmonics of the two AFPMVMs. It can be noticed that both AFPMVMs have the same main air-gap permeance harmonics, which are 0^{th}, 12^{th} and 24^{th}, respectively. The normalized values of the main air-gap permeance harmonics of the existing and proposed AFPMVMs are summarized in Table 2. The 0^{th} air-gap permeance harmonic can be reduced from 1 to 0.957 with the proposed separation slot design. Compared with the existing AFPMVM, the proposed AFPMVM can achieve a 5.9% increase in the amplitude of the 12^{th} air-gap permeance harmonic, which can contribute to enhancing the air-gap field modulation effect. Meanwhile, the 24^{th} air-gap permeance is reduced from 0.272 to 0.201.

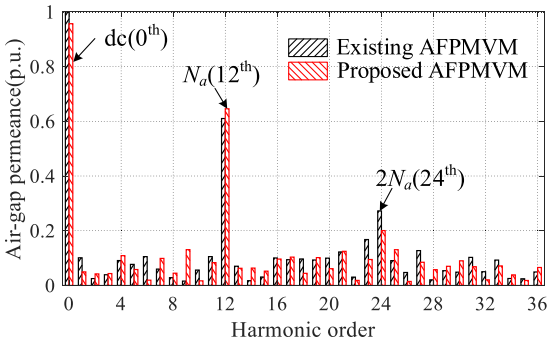

FIGURE 4. FFT spectrum of air-gap permeance distributions for two AFPMVMs.

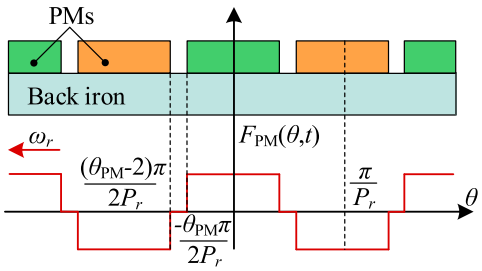

FIGURE 5. The simplified PM MMF model of the proposed AFPMVM.

TABLE 2. Main air-gap permeance harmonic for two AFPMVMs.

Air-gap permeance (p.u.)	Existing AFPMVM	Proposed AFPMVM
dc component	1	0.957
12^{th} harmonic	0.61	0.646
24^{th} harmonic	0.272	0.201

B. PM AND ARMATURE REACTION FIELD HARMONICS ANALYSIS

The air-gap flux density is derived from the interaction between primitive MMFs and air-gap permeance modulation function. The simplified PM MMF model of the AFPMVMs is shown in Fig. 5. It can be seen that the PM MMF rotates relative to the armature stator in the stationary coordinate system. Thus, the Fourier series expansion of the PM MMF can be expressed as

$$\begin{cases} F_{\text{PM}}\left(\theta, t\right) = \displaystyle\sum_{n=1,3,5\ldots}^{\infty} F_{\text{PM}n} \cos\left[nP_r\left(\omega_r t - \theta - \theta_0\right)\right] \\ F_{\text{PM}n} = \dfrac{4F_{\text{PM}}}{n\pi} \sin\left(n\pi\dfrac{\theta_{\text{PM}}}{2}\right) = \dfrac{4B_r h_m}{n\pi\mu_0\mu_r} \sin\left(n\pi\dfrac{\theta_{\text{PM}}}{2}\right) \end{cases} \tag{9}$$

where ω_r represents the rotor mechanical angular speed, θ_0 is the initial rotor position, $F_{\text{PM}n}$ represents the amplitudes of the n^{th} MMF harmonic generated by PMs, B_r is the remanence of PMs, h_m is the thickness of PMs, μ_0 is vacuum permeability, μ_r is the relative permeability of PMs, θ_{PM} is the PM pole arc coefficient.

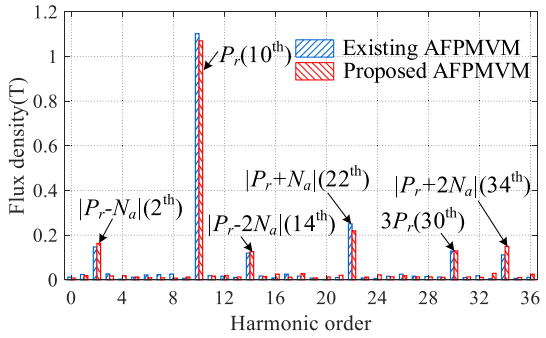

FIGURE 6. FFT spectrum of PM field distributions for two AFPMVMs.

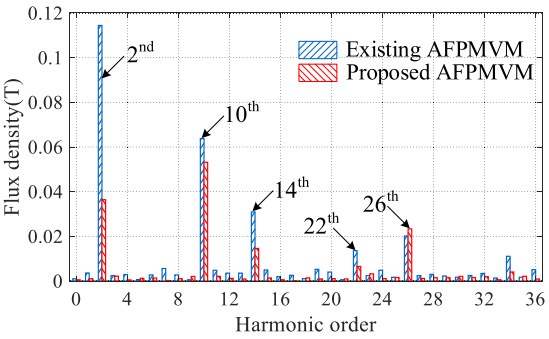

FIGURE 7. FFT spectrum of armature reaction field distributions for two AFPMVMs.

Based on the MMF-permeance method [1], the PM air-gap flux density in the proposed AFPMVM can be expressed as

$$\begin{aligned} B_{\mathrm{PM}}(\theta,t) &= F_{\mathrm{PM}}(\theta,t)\,\Lambda(\theta) \\ &= \sum_{n=1,3,5\ldots}^{\infty} F_{\mathrm{PM}n}\Lambda_0 \cos\left[nP_r(\omega_r t-\theta-\theta_0)\right] \\ &\quad + \sum_{n=1,3,5\ldots}^{\infty}\sum_{v=1,2,3\ldots}^{\infty} \frac{F_{\mathrm{PM}n}\Lambda_v}{2}\cos \\ &\quad \times\left[nP_r(\omega_r t-\theta_0)-(nP_r+vN_a)\theta\right] \\ &\quad + \sum_{n=1,3,5\ldots}^{\infty}\sum_{v=1,2,3\ldots}^{\infty} \frac{F_{\mathrm{PM}n}\Lambda_v}{2} \\ &\quad \times\cos\left[nP_r(\omega_r t-\theta_0)-(nP_r-vN_a)\theta\right] \end{aligned} \tag{10}$$

From (10), apart from the primitive PM MMF harmonic orders, i.e., $nP_r(n = 1, 3, 5, \ldots)$, various PM field harmonics with PPN of $|nP_r \pm vN_a|$ $(n = 1, 3, 5, \ldots, v = 1, 2, 3, \ldots)$, named as modulation harmonics, are modulated out by the armature stator as shown in Fig. 6. Theoretically, the order of PM field harmonics of the proposed AFPMVM is infinite because the combination of n and v is infinite. However, when $n > 3$ and $v > 1$, the corresponding amplitudes of the air-gap permeance harmonic and PM MMF harmonic are small enough to be neglected. Therefore, only $n = 1$ or 3 and $v = 1$ are taken into account when calculating the electromagnetic torque of the proposed AFPMVM.

To calculate the armature reaction MMF distribution of the proposed AFPMVM, the Fourier series of the winding

TABLE 3. Main parameters of existing machine and proposed machine.

Parameter	Harmonic order	Rotational direction
$i = 1$	$\lvert m\rvert$ (2nd)	Positive
	$\lvert m - N_a\rvert$ (10th)	Negative
	$\lvert m + N_a\rvert$ (14th)	Positive
$i = -5$	$\lvert m\rvert$ (10th)	Negative
	$\lvert m - N_a\rvert$ (22th)	Negative
	$\lvert m + N_a\rvert$ (2nd)	Positive
$i = 7$	$\lvert m\rvert$ (14th)	Positive
	$\lvert m - N_a\rvert$ (2nd)	Positive
	$\lvert m + N_a\rvert$ (26th)	Positive

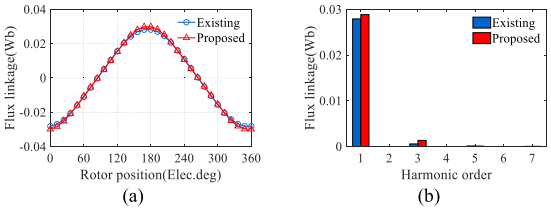

FIGURE 8. PM flux linkage comparison of two AFPMVMs. (a) PM flux linkage waveforms. (b) FFT spectrum.

function for each phase can be expressed as

$$\begin{cases} N_A = \sum\limits_{\substack{m=2i \\ i=1,3,5\ldots}}^{\infty} \dfrac{8N_c}{m\pi}\sin\left(\dfrac{m\pi}{12}\right)\cos(m\theta) \\ N_B = \sum\limits_{\substack{m=2i \\ i=1,3,5\ldots}}^{\infty} \dfrac{8N_c}{m\pi}\sin\left(\dfrac{m\pi}{12}\right)\cos\left[m\left(\theta-\dfrac{2\pi}{3}\right)\right] \\ N_C = \sum\limits_{\substack{m=2i \\ i=1,3,5\ldots}}^{\infty} \dfrac{8N_c}{m\pi}\sin\left(\dfrac{m\pi}{12}\right)\cos\left[m\left(\theta+\dfrac{2\pi}{3}\right)\right] \end{cases} \tag{11}$$

where N_c is coil turns number. Ignoring the harmonic components of armature current, the symmetrical three-phase currents can be expressed as

$$\begin{cases} i_A(t) = I\cos(\omega_e t+\varphi_0) \\ i_B(t) = I\cos\left(\omega_e t+\varphi_0-2\pi/3\right) \\ i_C(t) = I\cos\left(\omega_e t+\varphi_0+2\pi/3\right) \end{cases} \tag{12}$$

where I is the amplitude of phase current, φ_0 is the initial phase angle, $\omega_e = P_r\omega_r$. ω_e denotes electrical angular speed.

According to the winding function and three-phase current, the resultant armature reaction MMF can be calculated as

$$\begin{aligned} F_a(\theta,t) &= N_A(\theta)\,i_A(t)+N_B(\theta)\,i_B(t)+N_C(\theta)\,i_C(t) \\ &= \sum_{\substack{m=2i \\ i=1,-5,7\ldots}}^{\infty} \frac{12N_cI}{m\pi}\sin\left(\frac{m\pi}{12}\right)\cos \\ &\quad \times(\omega_e t-m\theta+\varphi_0) \end{aligned} \tag{13}$$

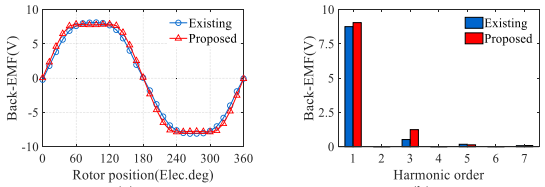

FIGURE 9. Back-EMF comparison of two AFPMVMs. (a) Back EMF waveforms. (b) FFT spectrum.

Similarly, the armature reaction air-gap flux density of the proposed AFPMVM can be expressed as

$$\begin{aligned} B_a(\theta,t) &= F_a(\theta,t)\,\Lambda(\theta) \\ &= \sum_{\substack{m=2i \\ i=1,-5,7\ldots}}^{\infty} \frac{12N_cI\Lambda_0}{m\pi}\sin\left(\frac{m\pi}{12}\right) \\ &\quad \times \cos(\omega_e t - m\theta + \varphi_0) \\ &\quad + \sum_{\substack{m=2i \\ i=1,-5,7\ldots}}^{\infty} \sum_{v=1,2,3\ldots}^{\infty} \frac{6N_cI\Lambda_v}{m\pi}\sin\left(\frac{m\pi}{12}\right) \\ &\quad \times \cos(\omega_e t - (m \pm vN_a)\,\theta + \varphi_0) \end{aligned} \tag{14}$$

From (13)-(14), it can be seen that the value of i not only determines the order of armature reaction field harmonics, but also determines the rotational directions of armature reaction field harmonics. The sources and rotational directions of the armature reaction field harmonic components are listed in Table 3. It can be observed that each harmonic in armature reaction field can be modulated out by different combinations of armature reaction MMF harmonics and air-gap permeance harmonics.

In order to confirm the analyses above, Fig. 7 shows the FFT spectrum of armature reaction field distributions for two AFPMVMs, in which the analysis results match well with finite-element analysis (FEA). Among which, 2nd, 10th, 14th, 22th, and 26th armature reaction field harmonics have high amplitudes due to high winding factor. Besides, the separation slot configuration can effectively weaken the 2nd harmonic of the armature reaction field, and has relatively little effect on the 10th harmonic of the armature reaction field. As a result, the 10th armature reaction field harmonic of the proposed AFPMVM has the highest amplitude.

IV. ELECTROMAGNETIC PERFORMANCE ANALYSIS

A. FLUX-LINKAGE AND BACK-EMF

Based on the MMF-permeance model established in Section II, the PM flux linkage of phase A can be expressed as

$$\begin{aligned} \psi_{\mathrm{PM}}(t) &= \int_{R_i}^{R_o}\left[\int_0^{2\pi} B_{\mathrm{PM}}(\theta,t)\,N_A(\theta)\,d\theta\right]rdr \\ &= \frac{R_o^2-R_i^2}{2}\int_0^{2\pi} B_{\mathrm{PM}}(\theta,t)\,N_A(\theta)\,d\theta \end{aligned} \tag{15}$$

where r is the air-gap radius, R_o and R_i are the stator outer radius, stator inner radius, respectively. Similar to the PM flux linkage, the armature reaction flux linkage of phase A can be expressed as

$$\begin{aligned} \psi_a(t) &= \int_{R_i}^{R_o}\left[\int_0^{2\pi} B_a(\theta,t)\,N_A(\theta)\,d\theta\right]rdr \\ &= \frac{R_o^2-R_i^2}{2}\int_0^{2\pi} B_a(\theta,t)\,N_A(\theta)\,d\theta \end{aligned} \tag{16}$$

According to (15) and Faraday's law of induction, the back-EMF of phase A can be calculated by

$$e_A(t) = -\frac{d}{dt}\left\{\int_{R_i}^{R_o}\left[\int_0^{2\pi} B_{\mathrm{PM}}(\theta,t)\,N_A(\theta)\,d\theta\right]rdr\right\} \tag{17}$$

The open-circuit PM flux linkage waveforms and FFT spectrum for both AFPMVMs are calculated and shown in Fig. 8. The fundamental component of the PM flux linkage of the proposed AFPMVM is about 3.3% large than that of the existing AFPMVM. Fig. 9 shows the open-circuit back EMFs of both AFPMVMs at the speed of 300 r/min. It can be seen that the proposed AFPMVM has higher fundamental component of back EMF than that of the existing AFPMVM. Besides, there are more odd order harmonic components in the back EMF of the two AFPMVMs, and the main harmonic component is the 3rd harmonic.

B. ELECTROMAGNETIC TORQUE

Based on the traditional electromagnetic theory, PM field harmonic and armature reaction field harmonic shared with the same PPN at the same rotational speed can be coupled with each other to generate the electromagnetic torque. The synthesized axial component B_z and tangential component B_t of the air-gap field harmonics can be expanded as

$$\begin{cases} B_z(\theta,t) = \sum_k B_{zk}\cos(k\theta - \theta_{zk}) \\ B_t(\theta,t) = \sum_k B_{tk}\cos(k\theta - \theta_{tk}) \end{cases} \tag{18}$$

where B_{zk} and θ_{zk} are the k^{th} Fourier coefficient and corresponding phase angle of B_z, respectively, B_{tk} and θ_{tk} are the k^{th} Fourier coefficient and corresponding phase angle of B_t, respectively.

To investigate the relationship between air-gap field harmonics and electromagnetic torque, the Maxwell stress tensor method is employed to obtain the contribution of each air-gap field harmonic to the electromagnetic torque. Hence, the electromagnetic torque of the proposed AFPMVM can be calculated based on the obtained axial component and tangential component of the air-gap field

$$T_e(t) = \int_{R_i}^{R_o}\int_0^{2\pi}\frac{r^2}{\mu_0}B_z(\theta,t)\,B_t(\theta,t)\,d\theta dr = \sum_k T_k(t) \tag{19}$$

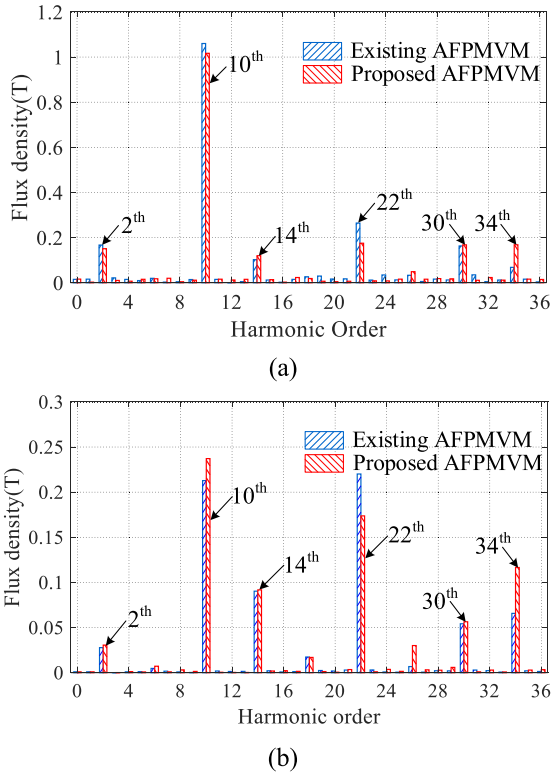

FIGURE 10. FFT spectrum of air-gap field distributions for two AFPMVMs. (a) Axial air-gap field harmonics. (b) Tangential air-gap field harmonics.

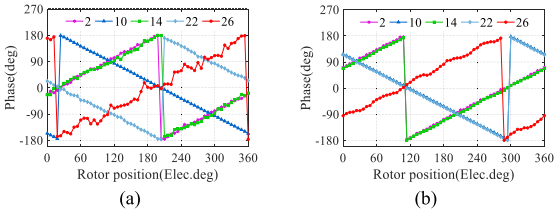

FIGURE 11. Phase angle of dominant air-gap field harmonics of the proposed AFPMVM versus rotor position. (a) Axial air-gap field harmonics. (b) Tangential air-gap field harmonics.

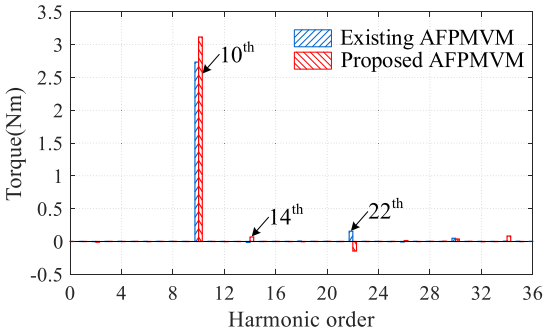

FIGURE 12. Torque contributions of the air-gap field harmonics.

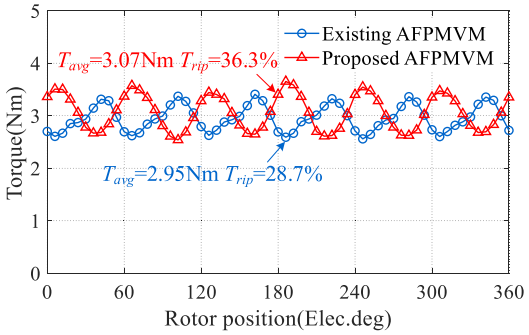

FIGURE 13. Electromagnetic torque comparison of two AFPMVMs.

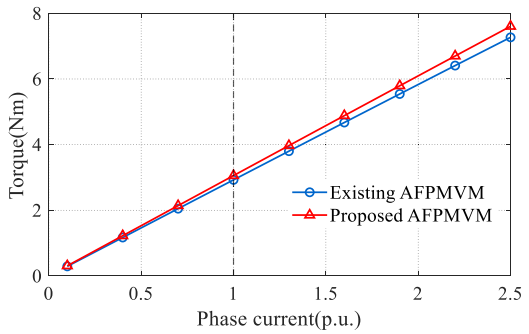

FIGURE 14. Variation of average torque with phase current.

where μ_0 is the vacuum permeability, T_k denotes the electromagnetic torque produced by the kth air-gap field harmonic, which can be deduced as

$$T_k(t) = \frac{\pi\left(R_o^3 - R_i^3\right)}{3\mu_0} B_{zk} B_{tk} \cos\left[\theta_{zk}(t) - \theta_{tk}(t)\right] \quad (20)$$

Under rated load condition, Fig. 10 gives the distribution of axial component and tangential component of the air-gap field harmonics of two AFPMVMs. The amplitude of the 10^{th} axial air-gap field harmonic is much larger than that of other axial air-gap field harmonics due to the higher amplitude of the 10th PM field harmonic. As shown in Fig. 7, it can be observed that both AFPMVMs have the same dominant armature reaction field harmonic orders, i.e., 2^{rd}, 10^{th}, 14^{th}, 22^{th}, and 26^{th}. Thus, these harmonic orders are taken as an example to investigate the variations of the air-gap field harmonics with respect to the rotor position. The phase angle of axial component and tangential component of the dominant air-gap field harmonic in the proposed AFPMVM versus rotor position is presented in Fig. 11. It can be seen that the rotational direction of the 10^{th} and 22^{th} air-gap field harmonics is opposite to that of the 2^{nd}, 14^{th}, and 26^{th} harmonics, which is consistent with the rotational direction of the armature reaction field harmonics derived from Table 3.

The contribution of each air-gap field harmonic to the electromagnetic torque is presented in Fig. 12. It can be found that only the 10^{th}, 14^{th}, and 22^{th} air-gap field harmonics are responsible for electromagnetic torque generation. Among which, the 10^{th} air-gap field harmonic exhibits the highest torque proportion in the both AFPMVMs, which can be defined as the air-gap field working harmonics. In addition, due to the high amplitude of the 10^{th} tangential air-gap field harmonic of the proposed AFPMVM, the 10^{th} air-gap field harmonic in the proposed AFPMVM contributes more for electromagnetic torque generation than that of the existing AFPMVM. It should be noted that the 22^{th} harmonic provides a positive torque component in the existing AFPMVM while a negative torque component in the proposed AFPMVM,

which is mainly due to the change in phase different between axial component and tangential component when the separation slot structure is adopted.

The comparison of electromagnetic torque between the two AFPMVMs is shown in Fig. 13. The average torques of the existing AFPMVM and proposed AFPMVM are 2.95 Nm and 3.07 Nm, respectively. Thus, the average torque increases by 4.1%. The torque ripples of the existing AFPMVM and proposed AFPMVM are 28.7% and 36.3%, respectively, which is mainly because the introduction of the separation slot increases the cogging torque. Fig. 14 shows the variation of average torque versus phase current of the existing and proposed AFPMVMs. It can be seen that the average torque of the proposed AFPMVM is larger than that of the existing AFPMVM under the same phase current.

C. POWER FACTOR

Based on the above analysis, the P_r (10^{th}) air-gap field harmonic is the working harmonic and provides the major torque component of AFPMVMs. However, the torque component generated by the P_a (2^{nd}) air-gap field harmonic is small enough to neglect and it can be defined as air-gap field non-working harmonic. Besides, the air-gap field harmonic is formed by the interaction of the PM field and armature reaction field harmonic with the same order. Hence, the armature reaction field can be rewritten as

$$B_a(\theta,t) = B_{aw}(\theta,t) + B_{an}(\theta,t) \tag{21}$$

$$B_{aw}(\theta,t) = \sum_{m=P_r}^{\infty} \frac{12N_c I\Lambda_0}{m\pi} \sin\left(\frac{m\pi}{12}\right) \cos(\omega_e t - m\theta + \varphi_0) + \sum_{|m\pm vN_a|=P_r}^{\infty} \sum_{v=1,2,3\ldots}^{\infty} \frac{6N_c I\Lambda_v}{m\pi} \sin\left(\frac{m\pi}{12}\right) \times \cos(\omega_e t - (m \pm vN_a)\theta + \varphi_0) \tag{22}$$

$$B_{an}(\theta,t) = \sum_{m\neq P_r}^{\infty} \frac{12N_c I\Lambda_0}{m\pi} \sin\left(\frac{m\pi}{12}\right) \cos(\omega_e t - m\theta + \varphi_0) + \sum_{|m\pm vN_a|\neq P_r}^{\infty} \sum_{v=1,2,3\ldots}^{\infty} \frac{6N_c I\Lambda_v}{m\pi} \sin\left(\frac{m\pi}{12}\right) \times \cos(\omega_e t - (m \pm vN_a)\theta + \varphi_0) \tag{23}$$

where B_{aw} is the armature reaction field working harmonic, B_{an} is the armature reaction field non-working harmonic.

According to (16), the armature reaction flux linkage can be divided into armature reaction working flux linkage ψ_{aw} and armature reaction non-working flux linkage ψ_{an}, the armature reaction flux linkage of phase A can be rewritten as

$$\begin{aligned}\psi_a(t) &= \psi_{aw}(t) + \psi_{an}(t) \\ &= \frac{R_o^2 - R_i^2}{2}\left[\int_0^{2\pi} B_{aw}(\theta,t) N_A(\theta)\, d\theta + \int_0^{2\pi} B_{an}(\theta,t) N_A(\theta)\, d\theta\right]\end{aligned} \tag{24}$$

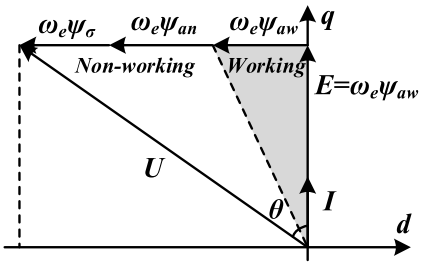

FIGURE 15. Phasor diagram of the proposed AFPMVM.

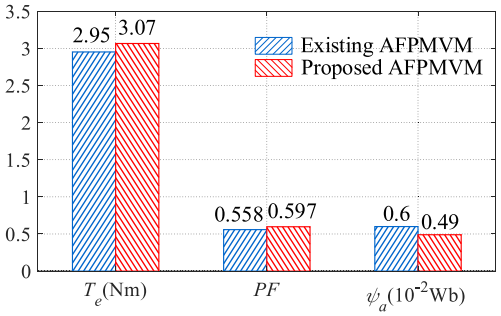

FIGURE 16. Comparisons of average torque, power factor, and armature reaction flux linkage between the two AFPMVM.

TABLE 4. Electromagnetic performance comparisons under rated conditions.

Parameters	Existing AFPMVM	Proposed AFPMVM
Average Torque (Nm)	2.95	3.07
Torque density (kNm/m^3)	11.93	13.29
Power factor	0.558	0.597
Armature reaction flux linkage (10^{-2}Wb)	0.6	0.49

It is noted that, from (24), both B_{aw} and B_{an} generate the fundamental armature reaction flux linkage. Therefore, the ψ_{aw} component and ψ_{an} component in the armature reaction flux linkage have the same order.

Fig. 15 shows the phasor diagram of the proposed AFPMVM. Under the control method of $I_d = 0$, the current phasor is in phase with the back-EMF phasor and the power factor angle is the same as the load angle. Therefore, the power factor can be expressed as

$$PF = \cos\theta = \frac{E}{U} = \frac{E}{\sqrt{E^2 + (\omega_e\psi_a + \omega_e\psi_\sigma)^2}} = \frac{1}{\sqrt{1 + \left[(\psi_{aw} + \psi_{an} + \psi_\sigma)/\psi_{\text{PM}}\right]^2}} \tag{25}$$

where ψ_σ denotes the leakage flux, E is the open-circuit back-EMF fundamental magnitude, U is the terminal voltage. It can be observed that the power factor is mainly determined by PM flux linkage, armature reaction flux linkage, and leakage flux. Since the PM flux linkage is limited by the property of PM material, the power factor can be effectively improved by reducing armature reaction flux linkage.

Considering that the armature reaction working flux linkage is the component contributing to electromagnetic torque, the armature reaction non-working flux linkage can be

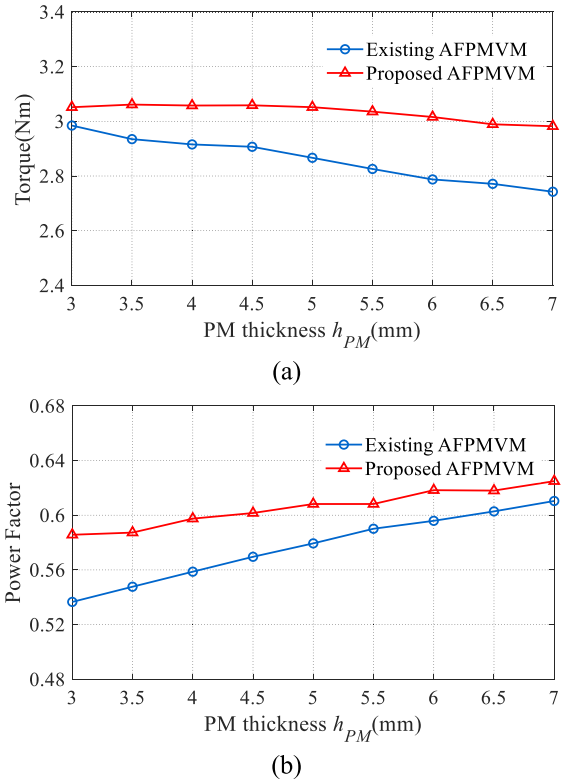

FIGURE 17. Influences of the PM thickness on the torque capability and power factor. (a) Average torque. (b) Power factor.

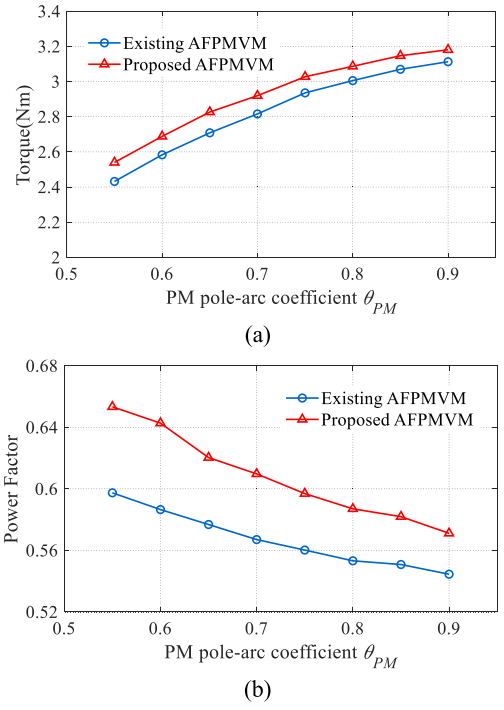

FIGURE 18. Influences of the PM pole-arc coefficient on the torque capability and power factor. (a) Average torque. (b) Power factor.

reduced to maintain the high torque and improve the power factor. In a large degree, this is mainly attributed to that the armature reaction field non-working harmonics have almost no contribution to electromagnetic torque. In PMVMs, the high-order harmonic of the armature reaction field, i.e., equal to P_r, is typically used to generate armature reaction working flux linkage. As a result, the armature reaction field non-working harmonics, e.g., equal to P_a, account for a large proportion of the armature reaction field due to the low-order of harmonics. This can explain why PMVMs exhibit relatively low power factor. As shown in Fig. 7, the 2nd armature reaction field harmonic of the existing AFPMVM exhibits the highest amplitude, which has a negative impact on the power factor and has almost no contribution to electromagnetic torque. In order to weaken the armature reaction field non-working harmonic that having long magnetic circuit, the separation slots are introduced in the armature stator of the proposed AFPMVM. It is evident from Fig. 7 that the 2nd armature reaction field harmonic is reduced from 0.114 T to 0.036T.

The comparisons of average torque, power factor, and armature reaction flux linkage are presented in Fig. 16 and listed in Table 4. It can be seen that the armature reaction flux linkage of the proposed AFPMVM is decreased 22.4% owing to decline of the armature reaction field non-working harmonic. Benefiting from the unique separation slot structure, the proposed AFPMVM exhibits 6.9% higher power factor than the existing AFPMVM.

V. INFLUENCES OF DESIGN PARAMETERS

Compared with the other design parameters, the PM thickness, PM pole-arc coefficient, and separation slot width exhibit more influence on the air-gap field harmonic distributions. Therefore, the influences of these design parameters on the electromagnetic torque and power factor are evaluated in order to reveal some design guidelines for the proposed AFPMVM.

A. PM THICKNESS

Fig. 17 analyzes the influences of PM thickness on the electromagnetic torque and power factor of both AFPMVMs. It can be seen that the average torques of both AFPMVMs slightly decrease with the increase of PM thickness. This phenomenon is due to the fact that the increase of PM thickness can lead to the increase the length of effective air-gap and the serious magnetic saturation of stator teeth. Meanwhile, it can be found that the power factors of both AFPMVMs increase as the PM thickness rises, as shown in Fig. 17(b), which is mainly due to the rising PM flux linkage. Compared with the existing AFPMVM, the electromagnetic performances of the proposed AFPMVM are much less sensitive to the PM thickness.

B. PM POLE-ARC COEFFICIENT

The PM pole-arc coefficient also has significant effect on electromagnetic performance of both AFPMVMs. The influences of PM pole-arc coefficient on electromagnetic torque and power factor are depicted in Fig. 18. It can be seen that the average torques rise with the increase of PM pole-arc coefficient, whereas the power factors are inverse to the PM

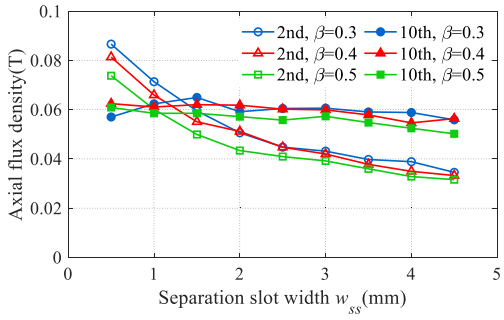

FIGURE 19. Influences of the separation slot width on the dominant axial armature reaction field harmonics under various β.

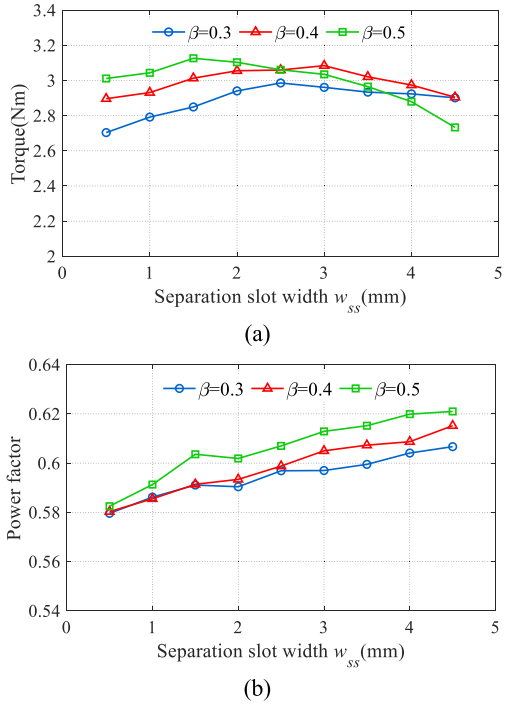

FIGURE 20. Influences of the separation slot width on the torque capability and power factor under various β. (a) Average torque. (b) Power factor.

pole-arc coefficient due to the increase in the leakage flux. In addition, it can be observed that there are larger average torque and higher power factor in the proposed AFPMVM compared to the existing AFPMVM under the same design parameters.

C. SEPARATION SLOT WIDTH

For the proposed AFPMVM, the air-gap field modulation effect is not only determined by the separation slots but also determined by the armature winding slots. Therefore, before analyzing the influence of separation slot width on electromagnetic performance, the armature winding slot width ratio need to be defined

$$\beta = \frac{\theta_{sa}}{2\pi / N_a} \tag{26}$$

The variations of the main axial armature reaction field harmonics with the separation slot width under various β are plotted in Fig. 19. It can be seen that the amplitude of the 2nd harmonic is sharply decreased with increasing the separation slot width, which is due to the enhancement of the low-order harmonic weakening effect in the separation slot. Meanwhile, the amplitude of 10th harmonic is also slightly decreased due to the decrease of dc component of air-gap permeance. The influences of the separation slot width on the electromagnetic torque and power factor are illustrated in Fig. 20(a) and (b), respectively. It can be observed that the average torques rise with the increase of separation slot first then drop. This is mainly attributed to the fact that the air-gap field modulation effect is enhanced with the increase of the separation slot width. However, as the separation slot width is higher than the optimal value, the magnetic saturation effect on the stator teeth results in the torque decrease. And, the power factor rises with the increase of the separation slot. This is mainly contributed by the fact that the non-working harmonic content of the armature reaction field is decreased.

VI. CONCLUSION

In this paper, a novel AFPMVM with modular stator is proposed to achieve higher power factor and larger torque density than the existing AFPMVM. An MMF-permeance model is established to reveal the modulation process of the air-gap field harmonics of the proposed machine. Then, the relationship between the electromagnetic torque and power factor of the proposed machine is investigated from the perspective of the air-gap field harmonics. It is indicated that the 10th air-gap field harmonic is the air-gap field working harmonic and provides the major electromagnetic torque of both AFPMVMs, whereas in the existing AFPMVM, the 2nd harmonic in the armature reaction field has the highest amplitude, which has a negative impact on the power factor and has almost no contribution to electromagnetic torque. Due to the weakening effect of the separation slots on low-order armature reaction field non-working harmonic, the proposed AFPMVM can achieve higher power factor and maintain high torque density. Compared to the existing AFPMVM, the electromagnetic torque and power factor of the proposed AFPMVM can be improved by 4.1% and 6.9%, respectively. Finally, the influences of some key design parameters on the electromagnetic performance of the proposed AFPMVM are analyzed and verified by finite element analysis.

REFERENCES

[1] T. A. Lipo and A. Toba, "Generic torque-maximizing design methodology of surface permanent-magnet Vernier machine," *IEEE Trans. Ind. Appl.*, vol. 36, no. 6, pp. 1539–1546, Nov./Dec. 2000.

[2] H. Zhou, W. Tao, C. Zhou, Y. Mao, G.-J. Li, and G. Liu, "Consequent pole permanent magnet Vernier machine with asymmetric air-gap field distribution," *IEEE Access*, vol. 7, pp. 109340–109348, 2019.

[3] L. Fang, D. Li, X. Ren, and R. Qu, "A novel permanent magnet Vernier machine with coding-shaped tooth," *IEEE Trans. Ind. Electron.*, vol. 69, no. 6, pp. 6058–6068, Jun. 2022.

[4] X. Zhao, S. Niu, and W. Fu, "A novel Vernier reluctance machine excited by slot PMs and zero-sequence current for electric vehicle," *IEEE Trans. Magn.*, vol. 55, no. 6, pp. 1–5, Jun. 2019.

[5] A. Ahmed and I. Husain, "Power factor improvement of a transverse flux machine with high torque density," *IEEE Trans. Ind. Appl.*, vol. 54, no. 5, pp. 4297–4305, Sep./Oct. 2018.

[6] T. Zou, D. Li, C. Chen, R. Qu, and D. Jiang, "A multiple working harmonic PM Vernier machine with enhanced flux-modulation effect," *IEEE Trans. Magn.*, vol. 54, no. 11, pp. 1–5, Nov. 2018.

[7] B. Kim and T. A. Lipo, "Operation and design principles of a PM Vernier motor," *IEEE Trans. Ind. Appl.*, vol. 50, no. 6, pp. 3656–3663, Nov./Dec. 2014.

[8] G. Liu, H. Zhong, L. Xu, and W. Zhao, "Analysis and evaluation of a linear primary permanent magnet Vernier machine with multiharmonics," *IEEE Trans. Ind. Electron.*, vol. 68, no. 3, pp. 1982–1993, Mar. 2021.

[9] D. Li, R. Qu, J. Li, and W. Xu, "Consequent-pole toroidal-winding outer-rotor Vernier permanent-magnet machines," *IEEE Trans. Ind. Appl.*, vol. 51, no. 6, pp. 4470–4481, Nov./Dec. 2015.

[10] J. Li, K. T. Chau, J. Z. Jiang, C. Liu, and W. Li, "A new efficient permanent-magnet Vernier machine for wind power generation," *IEEE Trans. Magn.*, vol. 46, no. 6, pp. 1475–1478, Jun. 2010.

[11] W. Zhao, Q. Hu, J. Ji, Z. Ling, and Z. Li, "Torque generation mechanism of dual-permanent-magnet-excited Vernier machine by air-gap field modulation theory," *IEEE Trans. Ind. Electron.*, vol. 70, no. 10, pp. 9799–9810, Oct. 2023.

[12] T. Jiang, W. Zhao, and L. Xu, "Analysis of split-tooth stator PM Vernier machines with zero-sequence current excitation," *IEEE Trans. Ind. Electron.*, vol. 70, no. 2, pp. 1229–1238, Feb. 2023.

[13] L. Xu, W. Zhao, M. Wu, and J. Ji, "Investigation of slot–pole combination of dual-permanent-magnet-excited Vernier machines by using air-gap field modulation theory," *IEEE Trans. Transport. Electrific.*, vol. 5, no. 4, pp. 1360–1369, Dec. 2019.

[14] Y. Liu, H. Y. Li, and Z. Q. Zhu, "A high-power factor Vernier machine with coil pitch of two slot pitches," *IEEE Trans. Magn.*, vol. 54, no. 11, pp. 1–5, Nov. 2018.

[15] J. Zhu, Y. Zuo, H. Chen, J. Chen, and C. H. T. Lee, "Deep-investigated analytical modeling of a surface permanent magnet Vernier motor," *IEEE Trans. Ind. Electron.*, vol. 69, no. 12, pp. 12336–12347, Dec. 2022.

[16] D. Wu, Z. Xiang, X. Zhu, L. Quan, M. Jiang, and Y. Liu, "Optimization design of power factor for an in-wheel Vernier PM machine from the perspective of air-gap harmonic modulation," *IEEE Trans. Ind. Electron.*, vol. 68, no. 10, pp. 9265–9276, Oct. 2021.

[17] Y. Yu, Y. Pei, and F. Chai, "Power factor analysis in spoke-type permanent magnet Vernier motors with different slot–pole combinations for in-wheel direct drive," *IEEE Trans. Transport. Electrific.*, vol. 9, no. 1, pp. 642–655, Mar. 2023.

[18] Y. Zhao, D. Li, X. Ren, and R. Qu, "Investigation of permanent magnet Vernier machines from armature field perspective," *IEEE J. Emerg. Sel. Topics Power Electron.*, vol. 10, no. 3, pp. 2934–2945, Jun. 2022.

[19] L. Xu, W. Wu, and W. Zhao, "Airgap magnetic field harmonic synergetic optimization approach for power factor improvement of PM Vernier machines," *IEEE Trans. Ind. Electron.*, vol. 69, no. 12, pp. 12281–12291, Dec. 2022.

[20] D. Li, R. Qu, and T. A. Lipo, "High-power-factor Vernier permanent-magnet machines," *IEEE Trans. Ind. Appl.*, vol. 50, no. 6, pp. 3664–3674, Nov. 2014.

[21] Y. Shi and T. W. Ching, "Power factor analysis of dual-stator permanent magnet Vernier motor with consideration on turn-number assignment of inner and outer stator windings," *IEEE Trans. Magn.*, vol. 57, no. 2, pp. 1–5, Feb. 2021.

[22] Y. Zhao, X. Ren, X. Fan, D. Li, and R. Qu, "A high power factor permanent magnet Vernier machine with modular stator and yokeless rotor," *IEEE Trans. Ind. Electron.*, vol. 70, no. 7, pp. 7141–7152, Jul. 2023.

[23] S. Xie, Y. Zuo, H. Chen, L. Cao, X. Yuan, B. S. Han, C. C. Hoang, and C. H. T. Lee, "Investigation on stator shifting technique for permanent magnet Vernier machines with two-slot pitch winding," *IEEE Trans. Ind. Electron.*, vol. 70, no. 7, pp. 6585–6596, Jul. 2023.

[24] J. Yang, G. Liu, W. Zhao, Q. Chen, Y. Jiang, L. Sun, and X. Zhu, "Quantitative comparison for fractional-slot concentrated-winding configurations of permanent-magnet Vernier machines," *IEEE Trans. Magn.*, vol. 49, no. 7, pp. 3826–3829, Jul. 2013.

[25] D. Li, T. Zou, R. Qu, and D. Jiang, "Analysis of fractional-slot concentrated winding PM Vernier machines with regular open-slot stators," *IEEE Trans. Ind. Appl.*, vol. 54, no. 2, pp. 1320–1330, Mar. 2018.

[26] R. Zhang, J. Li, R. Qu, and D. Li, "Analysis and design of triple-rotor axial-flux spoke-array Vernier permanent magnet machines," *IEEE Trans. Ind. Appl.*, vol. 54, no. 1, pp. 244–253, Jan./Feb. 2018.

[27] Y. Ma and W. N. Fu, "Design and comparison of Vernier permanent-magnet machines with different winding types based on fractional-slot windings," *IEEE Trans. Magn.*, vol. 57, no. 6, pp. 1–5, Jun. 2021.

[28] Z. Q. Zhu and Y. Liu, "Analysis of air-gap field modulation and magnetic gearing effect in fractional-slot concentrated-winding permanent-magnet synchronous machines," *IEEE Trans. Ind. Electron.*, vol. 65, no. 5, pp. 3688–3698, May 2018.

[29] Y. Li, H. Yang, H. Lin, W. Liu, and X. Zhao, "Torque generation mechanism and performance evaluation of a dual-sided PM machine with stator U-shaped magnets," *IEEE Trans. Ind. Appl.*, vol. 58, no. 1, pp. 250–260, Jan./Feb. 2022.

[30] Y. Li, H. Yang, H. Lin, L. Qin, and S. Lyu, "Investigation of double-side field modulation mechanism in consequent-pole PM machines with concentrated windings," *IEEE Trans. Energy Convers.*, vol. 36, no. 3, pp. 1635–1648, Sep. 2021.

[31] T. Zou, D. Li, R. Qu, J. Li, and D. Jiang, "Analysis of a dual-rotor, toroidal-winding, axial-flux Vernier permanent magnet machine," *IEEE Trans. Ind. Appl.*, vol. 53, no. 3, pp. 1920–1930, May/Jun. 2017.

GONGDE YANG was born in Henan, China, in 1988. He received the Ph.D. degree in electrical engineering from Southeast University, Nanjing, China, in 2019.

He is currently an Associate Professor with the School of Electrical Engineering and Automation, Fuzhou University, Fuzhou, China. His research interests include the design, analysis and control of permanent magnet machines, and power electronic technology and its industrial application.

JIE LI was born in Fujian, China, in 1999. He received the B.Eng. degree in electrical engineering from Henan Polytechnic University, Jiaozuo, China, in 2021. He is currently pursuing the master's degree with Fuzhou University, Fuzhou, China. His major research interest includes the design and optimization of permanent magnet machines.

MINGYAO LIN (Member, IEEE) received the B.S., M.S., and Ph.D. degrees in electrical engineering from Southeast University, Nanjing, China, in 1982, 1985, and 1995, respectively.

In 1985, he joined the School of Electrical Engineering, Southeast University, where he has been a Professor in electrical machines and control systems, since 2004. In 2002, he was a Visiting Scholar with the Esslingen University of Applied Sciences, Esslingen, Germany.